OPEN ACCESS

University of Dundee

University of Dundee

Modelling of Short-Term Interactions Between Concrete Support and the Excavated Damage Zone Around Galleries Drilled in Callovo–Oxfordian Claystone

Argilaga, Albert; Collin, Frèdèric; Lacarrière, Laurie; Charlier, Robert; Armand, Gilles; Cerfontaine, Benjamin

Published in:
International Journal of Civil Engineering

DOI:
10.1007/s40999-018-0317-9

Publication date:
2019

Document Version
Peer reviewed version

Link to publication in Discovery Research Portal

Citation for published version (APA):
Argilaga, A., Collin, F., Lacarrière, L., Charlier, R., Armand, G., & Cerfontaine, B. (2019). Modelling of Short-Term Interactions Between Concrete Support and the Excavated Damage Zone Around Galleries Drilled in Callovo–Oxfordian Claystone. *International Journal of Civil Engineering*, *17*(1), 1-18. https://doi.org/10.1007/s40999-018-0317-9

General rights
Copyright and moral rights for the publications made accessible in Discovery Research Portal are retained by the authors and/or other copyright owners and it is a condition of accessing publications that users recognise and abide by the legal requirements associated with these rights.

- Users may download and print one copy of any publication from Discovery Research Portal for the purpose of private study or research.
- You may not further distribute the material or use it for any profit-making activity or commercial gain.
- You may freely distribute the URL identifying the publication in the public portal.

Take down policy
If you believe that this document breaches copyright please contact us providing details, and we will remove access to the work immediately and investigate your claim.

Download date: 04. May. 2023

Author Accepted Manuscript of Argilaga, A, Collin, F, Lacarrière, L, Charlier, R, Armand, G & Cerfontaine, B 2019, 'Modelling of Short-Term Interactions Between Concrete Support and the Excavated Damage Zone Around Galleries Drilled in Callovo–Oxfordian Claystone', International Journal of Civil Engineering, vol. 17, no. 1, pp. 1-18. https://doi.org/10.1007/s40999-018-0317-9

Noname manuscript No.
(will be inserted by the editor)

Modelling of short-term interactions between concrete support and the excavated damage zone around galleries drilled in Callovo-Oxfordian claystone

Received: date / Accepted: date

Highlights

1. Excavation process of a gallery is modelled through a fully coupled model including concrete hydration, rock hardening/softening, water flow, desaturation and permeability evolution with deformation
2. A good compromise between convergence of the gallery and limited stress development in support concrete can be achieved by optimising the application moment of sprayed concrete and the use of deformable wedges
3. The strain localisation pattern around the gallery strongly depends on the concrete support solution used

Abstract Production of energy from nuclear power plants generates high-level radioactive nuclear waste, harmful during dozens of thousand years. Deep geological disposal of nuclear waste represents a reliable solutions for its safe isolation. Confinement of radioactive wastes relies on the multi-barrier concept in which isolation is provided by a series of engineered (canister, backfill) and natural (host rock) barriers. Few underground research laboratories have been built all over the world to test and validate storage solutions. The drilling of disposal drifts may generate cracks, fractures/strain localisation in shear bands within the rock surrounding the gallery especially in argillaceous rocks. These degradations affect the hydro-mechanical properties of the material, such as permeability, e.g. creating a preferential flow path for radionuclide migration. Hydraulic conductivity increase within this zone must remain limited to preserve the natural barrier. In addition galleries are currently reinforced by different types of concrete supports such as shotcrete and/or prefab elements. Their purpose is twofold: avoiding partial collapse of the tunnel during drilling operations and limiting convergence of the surrounding rock. Properties of both concrete and rock mass are time dependent, due to shotcrete hydration and hydromechanical couplings within the host rock. By the use of a hydro-mechanical coupled Finite Element Code with a Second Gradient regularization, this paper aims at investigating and predicting support and rock interactions (convergence, stress field). The effect of shotcrete hydration evolution, spraying time and use of compressible wedges is studied in order to determine their relative influence.

Keywords Nuclear waste · FEM modelling · COX · Numerical modelling · Sprayed concrete

Address(es) of author(s) should be given

1 Introduction

Nuclear power has been an important source of energy since its introduction more than half century ago [1]. The operation of atomic plants implies the generation of nuclear waste which is harmful to living organisms. This waste, which has a half-life usually much longer than the human life scale, supposes an important environmental risk. Therefore, it must be isolated from the biosphere. Since, at the present date, there are no available techniques to eliminate the back-end nuclear waste [24], different technical solutions to store this waste are considered [2]. Surface, shallow and deep geological repositories can host waste with different harmful levels.

The disposal of higher activity waste in deep underground repositories has been studied for a long while [2]. These repositories are designed to delay the radionuclides migration on a time-scale consistent with the radioactive decay period, thereby avoiding to affect

the biosphere. A multi-barrier solution ensures the isolation of the contaminants from the biosphere. They are firstly vitrified, then they are placed in steel canisters, which are in turn possibly placed in concrete containers or in a bentonite engineered barrier. Finally, the containers are placed in underground structures, with the last and highest level barrier being the natural geological formation.
The present work lies in the context of long-lived intermediate-level waste (MAVL) storage. The MAVL galleries consist in several hundred meters length, 10.4 m diameter, and structural concrete support ensuring stability. A layer of shotcrete is sprayed after excavation to ensure stability and an in-situ casted concrete ring is installed later. The shotcrete thickness is 0.20m and the in-situ casted concrete is 0.80m making a total thickness of 1m [3].

Argillaceous rocks [25] are envisaged as low-permeability host materials for the geological repositories and a particular attention is paid to the Callovo-Oxfordian claystone (COX) which is the geological medium envisaged in France by the national radioactive waste management agency ANDRA [3]. An Underground Research Laboratory (URL) is already built in the Meuse department to study underground solutions and the Callovo-Oxfordian formation [3]. This material was shown to exhibit inherent anisotropic behaviour typical of sedimentary materials. This structure can lead to the creation of weakness planes called bedding planes due to the diagenetic process [6].

Drilling generates an excavation damaged zone (EDZ) around galleries, characterized by the presence of fractures. In this zone, the hydraulic permeability is inhomogeneous and can severely increase up to several orders of magnitude, especially due to the presence of interconnected extensional fractures [4]. This increase has been highlighted by measurements performed under saturated conditions in boreholes drilled around the galleries in different orientations [4].

Constitutive models for the COX developed in ULiège take into account several transverse anisotropies: in situ stress state, elastic moduli, saturated permeability and plastic strength. This is achieved by the use of a fabric tensor that influences the cohesion [48]. Classical elasto-plastic models like Drucker Prager and Van Eekelen with cohesion softening reproduce correctly short term behaviour of the EDZ. However a visco-plastic framework is necessary to capture the long-term effects. In addition permeability changes are linked to the shear plastic deformation, significantly high inside strain localisation zones, in order to reproduce damage of the host rock [46].
Classical mechanics theories applied to strain localisation lead to a ill-posed posed problem. Therefore the local Second Gradient is introduced to regularise the problem [21]. It is based on microstructural considerations and avoids the pathological mesh dependency by introducing a second gradient coefficient, implicitly representing an internal length. Its local formulation allows its implementation in classical finite element framework.

During the excavation process, shotcrete or sprayed concrete is used to support and secure fresh areas of hard rock against downfall of small blocks. The hardening concrete layer creates a circular support modifying the gallery convergence [42].
Contrary to ordinary cast concrete, shotcrete is projected onto the hard rock. Subsequently its quality depends on many factors such as type of rock, rock surface, projection method (wet or dry) and skill of the worker [8]. Composition of the shotcrete is also slightly different from ordinary concrete. Indeed the water to cement ratio may be higher to ease the application, fibres (steel, glass or synthetic) may be added to increase ductility [36,8] and accelerators are added to fasten hardening [57]. Consequently, although ordinary concrete and shotcrete have similar composition, they behave in different manners. The long-term strength is especially lower for shotcrete [36,57,9].

Concrete hydration starts as soon as cement and water are in contact. Its state switches from a viscous liquid to solid and mechanical properties evolve very rapidly [15,16]. During this phase, the material is termed early age concrete and is subject to different physical phenomena. Firstly the hydration strongly increases its strength and stiffness properties [22]. Secondly autogenous shrinkage results from the chemical reaction [53]. Finally the exothermic reaction generates a temperature increase, which in turn speeds up the hydration [37].
Interactions between concrete and the environment affect the kinetic of hydration. Water exchange with surrounding air or rock mass may lead to drying of the concrete and crack generation [37]. In addition, while loaded, concrete is subject to short-term visco-elastic deformation to the micro-diffusion of water [7], termed basic creep. This creep rate decreases with the age of concrete [29].

Some models were proposed to simulate explicitly the hydration reaction within the concrete. [54] proposes a model taking the microstructure evolution into account but is cumbersome to solve at the scale of a case study. Some simplified physically-based relations are proposed in [11,37] to hydration degree evolution based on temperature variation, water availability and

interaction between different chemical species.
Some other models only approximate the evolution of hydration degree through a simplified relation and relate the variation of mechanical properties (strength or elastic modulus) or creep [23,22]. The most recent ones couple a simplified relation for hydration with creep, shrinkage and mechanical behaviours [52,27,32,51]. Creep is taken into account by combining Kelvin-Voigt and Maxwell rheological models [12]. Mechanical models may be based on damage mechanics [5,12] or elastoplasticity [40,32].
Some of these models were applied to tunnelling case studies [31]. They have shown that progressive hydration and creep significantly affect the stress distribution within the lining or convergence of the galleries [26]. Finally Buffo-Lacarriere and Sellier [10] apply their model to the simulation of nuclear waste repository from early age to one million years.

Concrete hydration and strain localisation modelling in rock materials are two distinct fields of research, generally treated separately. Advanced constitutive models were developed for both of them, but have never been applied within a single study. Nonetheless concrete support and the surrounding rock interact. Hydration and hardening of shotcrete restrain convergence of the gallery [42]. Subsequently the strain localisation process and EDZ expansion are modified, reducing permeability increase. In turn, rock pressure onto the concrete annulus generates radial stresses that must remain limited in order to avoid the failure of the support.
The objective of this paper is to study the effects of the support and especially shotcrete (application timing, kinetics) on the EDZ development during the early stage of construction. The originality of this work lies in modelling of shotcrete hardening through an advanced model together with the second-gradient framework to capture accurately strain-localisation. The influence of several parameters on the gallery deformation is directly linked to the strain-localisation process. Some recommendations related to important support parameters (shotcrete application or kinetics, deformable wedge) are provided to help design of galleries.

The paper is organized as follows: in Section 2 the constitutive model is presented including all constitutive relations both for the rock and the early age concrete. In Section 3 the numerical implementation of the concrete model is presented. In Section 4 the numerical model of the MAVL gallery is presented with results including a reference simulation of a gallery excavation and parametric cases varying the hydration kinetics, application time and with deformable wedges. The geomechanics sign convention is used: compressive stress is taken as positive.

2 Constitutive model

In this section all the constitutive laws of the rock and the concrete are presented. A second gradient law is also described, this law has the objective of regularizing the problem.

2.1 Mechanical behaviour: host rock

The following is limited to orthotropic material since the COX in the underground repository exhibits horizontal bedding orientation.

2.1.1 Definition of the effective stress

The effective Cauchy stress in orthotropic axes ${}^\sharp\sigma'_{ij}$ for unsaturated and anisotropic materials reads

$$ {}^\sharp\sigma_{ij}{}' = {}^\sharp\sigma_{ij} - {}^\sharp b_{ij}\, S_{r,w}\, \mathrm{p}_w, \tag{1}$$

where σ_{ij} is the total stress tensor, b_{ij} is the anisotropic Biot coefficient, $S_{r,w}$ is the saturation degree and p_w is the pore water pressure. Considering the air compressibility, Richards assumptions (constant air pressure) are adopted in the following. They may be irrelevant in the particular case of low and ultralow permeable porous media but are considered here as a first approximation. The pore air pressure variations have been neglected and the air pressure is taken equal to the atmospheric pressure.
In addition, the linear momentum balance equation is written in terms of total stresses at the end of the step [41]. At contrary to another approach writing the equation in incremental form ([34,35]), there is no need to consider the pore pressure coefficient depending on suction.

The Biot coefficient is expressed in orthotropic axes ${}^\sharp$ according to [18]

$$ {}^\sharp b_{ij} = \delta_{ij} - \frac{\mathrm{C}^e_{ijkl}}{3\,\mathrm{K}_s}, \tag{2}$$

where δ_{ij} is the Kronecker symbol, K_s is the bulk modulus of the solid phase (assumed homogeneous and isotropic at grain scale) and C^e_{ijkl} is the elastic stiffness tensor of the drained material. In cross-anisotropic conditions, only 5 independent parameters are necessary to describe this tensor.

These relations are formulated in the orthotropic axes. If global axes are not parallel to orthotropic axes, an adequate rotation is necessary to express the stress tensor and Biot coefficient in global axes, respectively σ_{ij} and b_{ij} [44].

The mechanical model considers instantaneous elastic ϵ^e_{ij} and plastic ϵ^p_{ij} deformation as well as time-dependant plastic deformation ϵ^{vp}_{ij}. Therefore the total strain increment $\dot{\epsilon}_{ij}$ is defined as

$$\dot{\epsilon}_{ij} = \dot{\epsilon}^e_{ij} + \dot{\epsilon}^p_{ij} + \dot{\epsilon}^{vp}_{ij}. \tag{3}$$

Elasticity is assumed linear and defined in rate form:

$$^{\sharp}\dot{\sigma}'_{ij} = \mathrm{C}^e_{ijkl}\, ^{\sharp}\dot{\epsilon}^e_{kl}. \tag{4}$$

2.1.2 First gradient mechanical model

The elastoplastic material is characterised by an internal friction model and a Van Eekelen yield surface defined as [55]

$$F^p \equiv \mathrm{II}_{\hat{\sigma}} - m\left(\mathrm{I}_{\sigma'} + \frac{3c}{\tan\phi_c}\right) = 0, \tag{5}$$

where c is the cohesion, ϕ_c the friction angle, m the yield surface parameter, $\mathrm{I}_{\sigma'}$ the first invariant of the stress tensor and $\mathrm{II}_{\hat{\sigma}}$ the second invariant of the deviator stress tensor. A plot of the surface in the first and second stress tensor invariants is shown in Figure 1a. A dependency to the third invariant is also introduced and represented in Figure 1b.

It is demonstrated that cohesion and friction angle harden/soften upon loading [39,30]. In the following strength parameters evolve as a function of the Von Mises' equivalent deviatoric plastic strain

$$\epsilon^p_{eq} = \sqrt{\frac{2}{3}\hat{\epsilon}^p_{ij}\hat{\epsilon}^p_{ij}}, \tag{6}$$

where

$$\hat{\epsilon}^p_{ij} = \epsilon^p_{ij} - \frac{\epsilon^p_{kk}}{3}\delta_{ij}. \tag{7}$$

Therefore cohesion and friction angle are progressively modified according to

$$c = c_0 + \frac{(c_f - c_0)\,\hat{\epsilon}^p_{eq}}{B_c + \hat{\epsilon}^p_{eq}}, \tag{8}$$

$$\phi_e = \phi_{e,0} + \frac{(\phi_{e,f} - \phi_{e,i})\,\hat{\epsilon}^p_{eq}}{B_\phi + \hat{\epsilon}^p_{eq}}, \tag{9}$$

$$\phi_c = \phi_{c,0} + \frac{(\phi_{c,f} - \phi_{c,0})\,\hat{\epsilon}^p_{eq}}{B_\phi + \hat{\epsilon}^p_{eq}}, \tag{10}$$

where c_f is the maximum cohesion, c_0 is the initial cohesion, ϕ_f is the final friction angle, ϕ_0 is the initial friction angle, ϕ_c is the compression friction angle, ϕ_e is the extension friction angle and B_c/B_ϕ are material parameters ruling the rate of hardening/softening. Especially B_c/B_ϕ are the equivalent deviatoric plastic strain for which half of the hardening/softening is reached as depicted in Figure 1c.

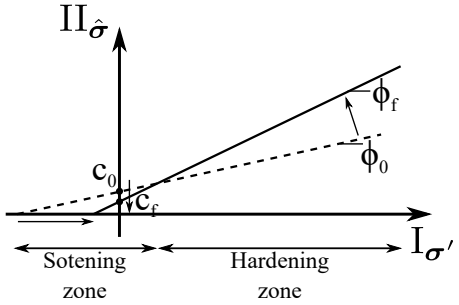

(a) Yield surface in effective stress invariant plane

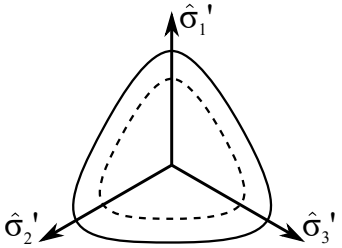

(b) Yield surface in deviatoric plane

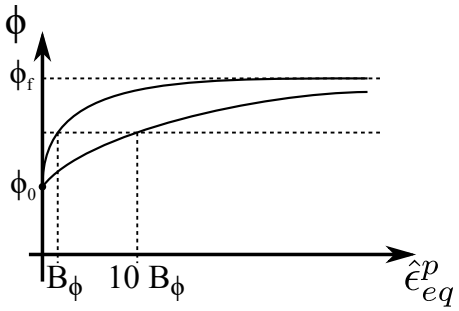

(c) Hardening of friction angle. $10B_\phi$ illustrates the effect of the hardening coefficient B_ϕ

Fig. 1: Ingredients of the constitutive model for rock material: yield surfaces and hardening rule

Anisotropy is known to influence strength parameters and was demonstrated not to be influenced by the mean stress. Subsequently it is assumed that only cohesion is affected by the angle between the loading direction and bedding orientation [44]. This is introduced into the constitutive law by using a second order microstructure fabric tensor a_{ij} [49,17]. Physically this tensor may characterise the arrangement of intergranular contacts (particles assembly) or describe the distribution of voids and cracks.

2.1.3 Viscoplasticity

Creep deformation is modelled through a viscoplastic formulation based on developments proposed by [33, 58] for the analysis of the COX viscoplastic behaviour. There is no consistency condition enforced for the vis-

coplastic surface, F^{vp}. Therefore the stress state is allowed to go beyond it, $F^{vp} > 0$, as shown in Figure 2. Delayed hardening of the internal friction angle will progressively restore the condition, $F^{vp} = 0$. The viscoplastic flow rule is defined in [47].

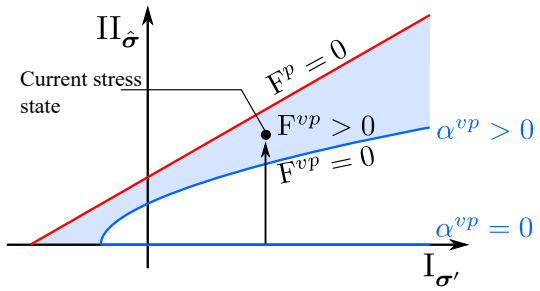

Fig. 2: Viscoplastic surface hardening. α_{vp} is a viscoplastic hardening function that affects F^{vp} [33,58].

The approach consists in a single viscoplastic mechanism decoupled from elastoplasticity. Creep increment of deformation $\dot{\epsilon}^{vp}$ is computed first at the beginning of a time step, then a new total deformation increment $\dot{\epsilon}'$ is computed such that:

$$\dot{\epsilon}' = \dot{\epsilon}^e + \dot{\epsilon}^p = \dot{\epsilon} - \dot{\epsilon}^{vp} \tag{11}$$

and used as an input for the elastoplastic constitutive law. Details of this implementation in the gallery excavation can be found in [45]. The choice of parameters should be adequate since the viscoplastic yield surface must remain inside the elastoplastic one.

2.1.4 Second gradient mechanical model

The second gradient model is introduced to tackle the localisation problem [20,44]. It adds microstructured material description by considering a continuum field in the micro-scale enriched by higher order terms [28]. In this model the micro-scale enriches the kinematics of the media introducing a local dependence on an internal length parameter. The introduced characteristic length regularizes the solution making it mesh independent [13], this allows to obtain objective solutions with strain localization.

2.2 Flow model

The liquid phase transfer by advection in an anisotropic medium is defined by the Darcy's law such that

$$f_{wi} = -\rho_w \frac{k_{w,ij}\, k_{rw}}{\mu_w} \left(\frac{\partial \mathrm{p}_w}{x_j} + \rho_w\, g_j \right) \qquad i,j = 1,3, \tag{12}$$

where k_{rw} is the relative permeability, g_j is the gravity vector component in direction j and $k_{w,ij}$ is an orthotropic permeability tensor. It is defined in the orthotropic axes $^\sharp k_{wij}$ and requires only two parameters to be defined: permeability values parallel $k_\parallel$ and perpendicular $k_\perp$ to the isotropic planes.

A retention curve and the evolution of relative permeability k_{rw} are defined to close the model. The first one is defined by the Van Genuchten's relation [56]

$$S_{rw} = S_{res} + (S_{max} - S_{res}) \left(1 + \left(\frac{\mathrm{p}_c}{P_r} \right)^{\frac{1}{1-\mathcal{M}}} \right)^{-\mathcal{M}} \tag{13}$$

where S_{res} and S_{max} are the residual and maximum water degrees of saturation, $\mathcal{M}$ is a model parameter, P_r is the Van Genuchten air entry pressure and p_c is the capillary pressure. Permeability curve is given by

$$k_{rw} = \sqrt{S_{rw}} \left(1 - \left(1 - S_{rw}^{\frac{1}{\mathcal{M}}} \right)^{\mathcal{M}} \right)^2 . \tag{14}$$

The permeability evolution around the gallery is not homogeneous due to the fracturation process. A dependency on deformation is introduced [46] to derive $k_\parallel$ and $k_\perp$.

2.3 Concrete behaviour

Modelling of concrete is considered from its projection onto the gallery wall to several weeks. During its early age, its properties change as it hydrates after being applied to the gallery walls [42]. An empirical relation is used in the finite element model to link pre-established hydration evolution to strength properties of the concrete. Hydration evolution is obtained by numerical means considering a homogeneous monoconstituent CEM I concrete in adiabatic conditions.

2.3.1 Hypotheses

The exact composition of the shotcrete not being known, a standard CEM I has been chosen as a reference and extrapolated to the investigated case study. We consider the hydration properties of a CEM I cement type which was calibrated against experimental results. Another set of parameter is investigated to reproduce a faster hydration behaviour, obtained for instance by adding accelerator additive.
In order to simplify the problem, we uncouple the hydration and excavation modelling. We consider on one hand the equations of concrete hydration in adiabatic

conditions. This hypothesis is deemed valid since heat and water exchange with atmosphere inside the tunnel are limited. Indeed, ventilation is activated only after several weeks. In addition water permeability of the surrounding COX is quite low, limiting water exchange. Finally the limited width of shotcrete (0.2m) and its fast application with respect to hydration kinetics ensures that the hydration reaction can be considered homogeneous.
On the other hand, we simplify the mechanical behaviour of concrete during the excavation simulation. Shotcrete is assumed to be modelled by an elastoplatic constitutive law whose parameters depend on the evolution of the hydration degree. During its very early age (few hours), concrete behaves like a very viscous fluid rather than a solid and early age creep should be considered. However it does not really affect tunnel convergence during this period. Therefore we decide to discard any creep behaviour since no data are easily available to calibrate such a behaviour. Instead, properties of the concrete at very early age (before concrete starts hardening) are considered elastic with a very low stiffness, to ensure convergence is not affected.

2.3.2 Cement hydration

Hydration covers a set of very complex chemical reactions depending on many variables such as water content, nature of hydrates or temperature [11]. The hydration rate depends on two antagonistic phenomena. At the beginning, where only few solid hydrated phases have been produced, supersaturation of the interstitial solution speeds up the hydration kinetics by accelerating hydrate precipitation. On the other hand, as hydration progresses, anhydrous grains are surrounded by a growing hydrated layer. Diffusion of water to the anhydrous grain slows down as well as the hydration rate.
The global hydration reaction should take into account all of the reaction constituents interacting together. However in this case, only a clinker phase will be considered. Kinetic of the hydration degree α_c of this phase is described by the hydration reaction proposed in [11] such that

$$\dot{\alpha}_c = A\, \Pi(\bar{r}_m)\, c_a(\alpha_c, w_p)\, h(T), \tag{15}$$

where

- A [h^{-1}] is a fitting parameter linked to the acceleration of the reaction kinetics due to supersaturation;
- Π [-] models the water accessibility to anhydrous phase;
- c_a [-] deals with the chemical activation (linked to supersaturation of interstitial solution);
- h [-] represents the temperature influence.

The hydration degree α_c is used to derive the volumetric concentrations of hydrates and the anhydrous phase in the paste such that

$$C_{p,hydr} = R_c\, \alpha_c\, C_{p,anh,0} \tag{16}$$

$$C_{p,anh} = (1-\alpha_c)\, C_{p,anh,0} \tag{17}$$

$$\tag{18}$$

where R_c [-] is the ratio between hydrates and anhydrous phases and $C_{p,anh,0}$ [$\mathrm{m}^3/\mathrm{m}^3$] is the initial volumetric concentration of anhydrous phase

$$C_{p,anh,0} = \frac{m_{c0}}{V_{p,0}\, \rho_c} \tag{19}$$

in which $V_{p,0}$ [m^3] is the initial paste volume, m_{c0} [kg] is the initial mass of anhydrous phase and ρ_c [kg/m^3] is the anhydrous phase density. Thus the ratio between these two concentrations is a function of α_c and R_c only

$$\frac{C_{p,hydr}}{C_{p,anh}} = R_c \frac{\alpha_c}{1-\alpha_c}. \tag{20}$$

Water accessibility Π is a function of pseudo-distance $\bar{r}_m$ [-] defined over $[0, +\infty[$, representing the decreasing availability of free water for anhydrous grains and two fitting parameters B [-] and n [-]

$$\Pi = \exp\left(-B\, \bar{r}_m^n\right). \tag{21}$$

This accessibility is reduced by the decrease of water content w_p [-], paste porosity Φ_p [-] and by the increase/decrease of hydrate/anhydrous $C_{p,hydr}/C_{p,anh}$ volumetric concentration such that

$$\bar{r}_m = \frac{C_{p,hydr}}{w_p\, \Phi_p\, C_{p,anh}}. \tag{22}$$

Porosity Φ_p is defined according to

$$\begin{aligned}\Phi_p &= 1 - (C_{p,hydr} + C_{p,anh}) \\ &= 1 - C_{p,anh,0}\,(1 - \alpha_c + \alpha_c\, R_c).\end{aligned} \tag{23}$$

Therefore Eq. (22) is rewritten as

$$\bar{r}_m = R_c\, \frac{\alpha_c}{1-\alpha_c}\, \frac{1}{1 - C_{p,anh,0}\,(1-\alpha_c+\alpha_c\, R_c)}\, \frac{1}{w_p}. \tag{24}$$

Chemical activation c_a depends on the supersaturation of interstitial fluid. It is described as the ratio of the quantity of dissolved anhydrous to the water content

$$c_a = \frac{\alpha_c\, C_{p,anh,0}}{w_p} \tag{25}$$

Thermal activation h is taken into account through the Arrhenius law,

$$h = \exp\left(-\frac{E_a}{RT}\right), \tag{26}$$

where E_a [J/mol] is the activation energy of clinker phase, R [J/mol/K] the gas constant and T [K] the temperature.

2.3.3 Concrete strength

In the following we assume the uniaxial strength (f_c [MPa]) and stiffness (E [MPa]) are directly dependant on the hydration degree, as reported in [23]. However there exists a threshold $\alpha_{c,th}$ below which both strength and stiffness are null, namely the concrete behaves more like a viscous liquid. Above this threshold, their evolution reads

$$f_c(\alpha_c) = f_{c,f} \left(\frac{\alpha_c - \alpha_{c,th}}{1 - \alpha_{c,th}} \right)^a, \tag{27}$$

$$E(\alpha_c) = E_{c,f} \left(\frac{\alpha_c - \alpha_{c,th}}{1 - \alpha_{c,th}} \right)^b, \tag{28}$$

where $f_{c,f}$ and $E_{c,f}$ are the final strength and stiffness. The Poisson's ratio is deemed constant after the threshold. However from a numerical point of view, the stiffness cannot be null. Therefore it is assumed that the material behaves elastically if the hydration degree is below the threshold. Elastic properties are set low enough (with respect to rock properties) to avoid any significant restraint of convergence.

Finally the uniaxial strength f_c is linked to a Drucker-Prager model, depending on friction angle and cohesion. Therefore we assumed the friction angle ϕ_c is constant and equal to 45°. Cohesion evolves with hydration degree according to

$$c = f_c(\alpha_c) \left(\frac{3 - M}{M} \frac{\tan(\phi_c)}{3} \right), \tag{29}$$

$$M = \frac{6 \sin(\phi_c)}{3 - \sin(\phi_c)}. \tag{30}$$

3 Numerical implementation of the early age concrete model

Numerical modelling of the early age concrete is based on two steps. Firstly, the assumed adiabatic hydration reaction is discretised into Matlab to obtain the time evolution of the hydration degree. This serves as an input for the finite element modelling of the tunnel excavation, where mechanical properties of the concrete evolve with hydration degree.

Time discretisation of the adiabatic hydration reaction requires equations (15) to (26) and conservation equations (water mass and heat) to close the system. Therefore we obtain the following set of equations

$$\begin{cases} \Delta\alpha_c^t = & A\, \Pi(\bar{r}_m^t)\, c(\alpha_c^t, w_p^t)\, h(T^t) \\ \alpha_c^{t+1} = & \alpha_c^t + \Delta\alpha_c^t\, \Delta t \\ w_p^{t+1} = & w_p^0 - \alpha_c^{t+1}\, Q_{th}^w\, \dfrac{m_{c0}}{\rho_w\, V_{p,0}} \\ T^{t+1} = & T^t + \Delta\alpha_c^t\, \Delta t\, \dfrac{Q_{th}^T\, m_{c0}}{\rho_b\, c_b} \end{cases} \tag{31}$$

where ^{t} and $^{t+1}$ represent quantities at time step t or $t+1$, Δt [h] is the time step duration, Q_{th}^w [kg/kg] is the water mass needed for the hydration of 1kg of anhydrous phase, Q_{th}^T [J/kg] is heat released by the hydration of 1kg of anhydrous phase, ρ_w [kg/m^3] is density of water, ρ_b [kg/m^3] is the concrete density and c_b [J/kg/K] is the concrete heat capacity.

All parameters related to the composition or physical properties of concrete are reported in Tables 1 and 2. Two different cases were considered for the three fitting parameters and are described in Table 3. The standard case corresponds to the fitting of experimental results. Parameters of the accelerator case were chosen to speed up the hydration reaction. The initial variables are provided in Table 4.

Material	Content [kg/m^3]	Density [kg/m^3]
Cement	300	3500
Water	175	1000
Aggregate	1000	1379

Table 1: Concrete formulation

$Q_t^w h$ [kg/kg]	$Q_t^T h$ [kJ/kg]	R_c [-]	E_a/R [K^{-1}]	ρ_b [kg/m^3]	c_b [J/kg/K]
0.32	500	1.32	3500	2300	900

Table 2: Physical cement and concrete properties

	A [h^{-1}]	B [-]	n [-]
Standard	3.64	3.38	0.52
Accelerator	6.65	3.70	0.52

Table 3: Fitting parameters for the two considered cases

α_c [-]	w_p [-]	T [K]
$1 \cdot 10^{-6}$	0.6364	293

Table 4: Initial variables for concrete hydration

Results of hydration simulation corresponding to the parameters provided are described in Figures 3 and 4. After 50 days, hydration is almost 70% completed but half of it is reached after the first 2 days. Therefore we can reasonably assume that during this period, heat

and water exchanges with the ground and tunnel are limited. Subsequently adiabatic conditions are valid as well as the hydration solution.
The long-term validity of this relation for the tunnel case study is more questionable since conditions are not adiabatic any more and additional physical phenomena occur. In addition this relation cannot be validated against classical adiabatic tests since the heat released after a long time is too low to be accurately measured. However cement hydration continues within concrete. We assume the presented relation remains valid even if it probably diverges from reality. However this divergence should remain limited since most of the hydration occurs at the beginning of the reaction.

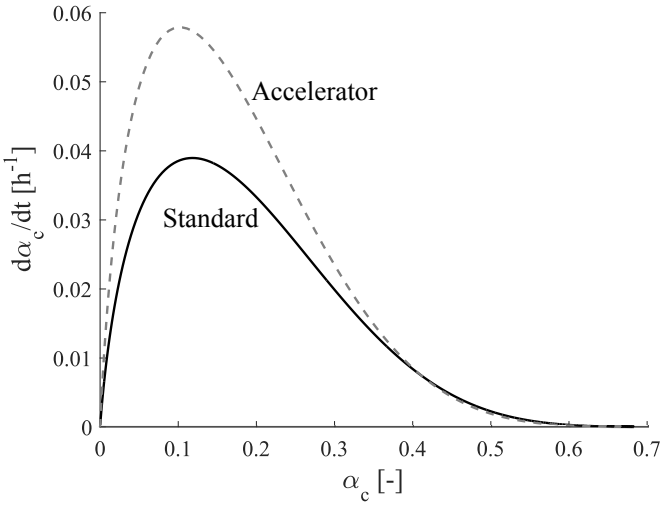

Fig. 3: Rate of hydration $\dot{\alpha}_c$ with respect to the hydration degree α_c, with or without accelerator

Strength evolution is based on the evolution of hydration degree with time as described by Equations (27)-(28). Related parameters are based on the work of [23]. The corresponding evolution of uniaxial compression f_c and Young modulus E is provided in Figures 5 and 6. As a consequence of the hydration degree evolution, mechanical parameters fast evolve to reach half of their final value after two days.
Strength starts to develop after the hydration threshold $\alpha_{c,th}$ is reached, namely after several hours. During this short amount of time, the shotcrete has theoretically no strength but behaves as a very viscous fluid. However we considered it as an elastic material whose stiffness is very low. Therefore error on the convergence evolution should remain limited.

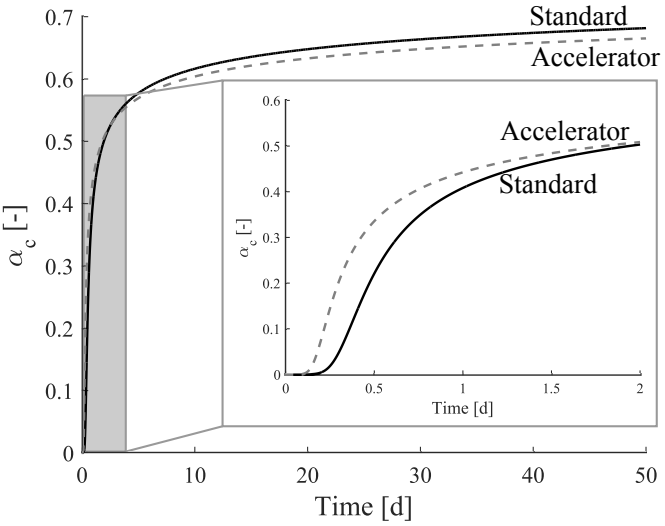

Fig. 4: Evolution of the hydration degree α_c with time, with or without accelerator

a [-]	b [-]	$\alpha_{c,th}$ [-]
0.84	0.26	0.25

Table 5: Parameters for strength evolution of the concrete

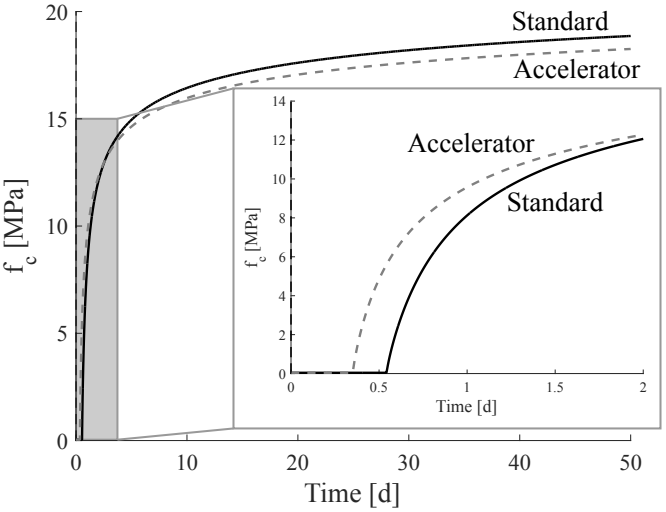

Fig. 5: Evolution of the uniaxial compression strength f_c with time

4 Numerical modelling of the excavation

In this section results are presented including a reference simulation and a parametric study. The reference simulation consists in the quarter of a gallery excavation with 20cm of sprayed shotcrete placed one day after excavation front reached the considered cross section. The shotcrete follows the hydration evolution defined

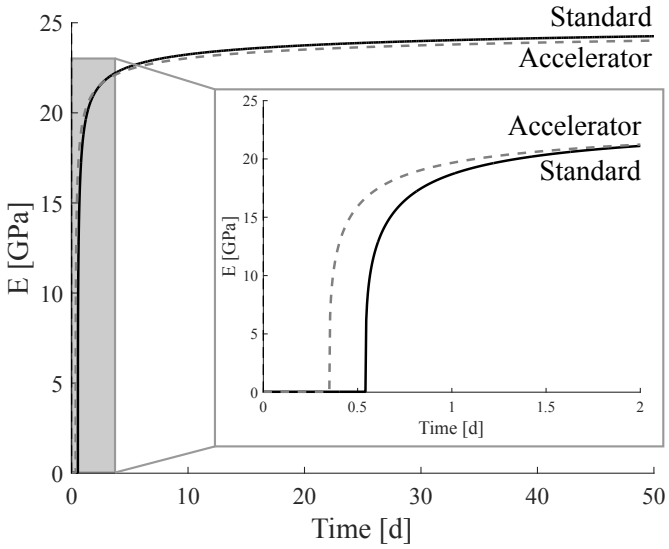

Fig. 6: Evolution of theYoung modulus E with time

in Figure 4. The reference simulations results are then compared to the parametric study results in order to highlight the effect of the different factors, namely accelerator agents in the concrete, time of the shotcrete spray and deformable wedges within the shotcrete liner.

4.1 Model parameters

A finite element code, Lagamine (ULiège) [14,19], is used to solve the boundary value problem of a gallery excavation, Figure 7. Given the symmetries of the problem only a quarter of the gallery is modelled. This results in a mesh with 7669 nodes, 2064 quadratic elements, and 28985 unknowns.

The initial conditions for the stresses and pore pressure are summarized in Table 6. Stresses and pore water pressures applied at the internal and external boundaries are defined as a function of time according to

$$\sigma(t) = \lambda(t)\sigma_0 \tag{32}$$

where σ_0 is a constant and $\lambda(t)$ is a time dependent multiplier. This multiplier is equal to one for the whole simulation along the external boundaries, assuming constant stress and pore water pressures. On the contrary the evolution of stress along the gallery wall is based on a deconfining curve [43], as shown in Figure 8. Origin of the time axis corresponds to the moment when the studied section starts to be influenced by excavation of previous sections of the tunnel. Pore water pressure starts to decrease towards atmospheric pressure when excavation front reaches the studied section. Shotcrete is sprayed one day after the section was excavated (day 16).

Ventilation of the galleries is also considered, the ventilation imposes a relative humidity of 70%, this modifies the hydraulic boundary condition in the gallery wall by reducing the pore pressure from $0Pa$ to $-49.1MPa$. Ventilation starts 35 days after the excavation starts, this is 20 days after the excavation front arrival, but the relative humidity is not instantaneously decreased from 100% to 70%, instead it is progressively reduced during a period of 3 months.

	Parameter	Value [MPa]
Total stress	$\sigma_{v,0}$	12.7
	$\sigma_{h,0}$	12.4
	$\sigma_{H,0}$	16.1
Pore pressure	$p_{w,0}$	12.4

Table 6: Initial total stress conditions and pore pressure

All physical parameters necessary in the aforementioned constitutive laws are reported in Table 7. Their determination is described in [44]. They are the basis for further simulations.

4.2 Reference simulation

Results are presented for a period of two months in the excavation time reference, the excavation front interception happens the 15th day and the spraying of shotcrete in the reference simulation one day after (16th day). This date is used as a zero time reference in the following. The two months time window is retained because the main coupled phenomena due to the excavation deconfinement and effect of the shotcrete happen before this time. Afterwards, deformation is governed by time dependent effects in the host rock rather than the shotcrete spraying time or hydration kinetics.

Restrained convergence induces the development of an effective normal pressure between shotcrete and the host rock. On average it is equal to $1.7MPa$ and $1.6MPa$ respectively in the vertical and horizontal directions at the end of the simulation. In turn the shotcrete orthoradial stress is $45.1MPa$ in the springline and $42.5MPa$ in the crown (Figure 9). Subsequently the whole concrete annulus is plastified while only few plasticity occurs within the rock, as could be observed in Figure 9. Taking viscoplasticity into account may have slightly reduced the orthoradial stress by allowing creep to take place. However such stress distribution is very high and may lead to failure of the sprayed concrete support. Two possible solutions exist to reduce it, namely the delay of spraying after excavation or the use of deformable wedges, are further investigated.

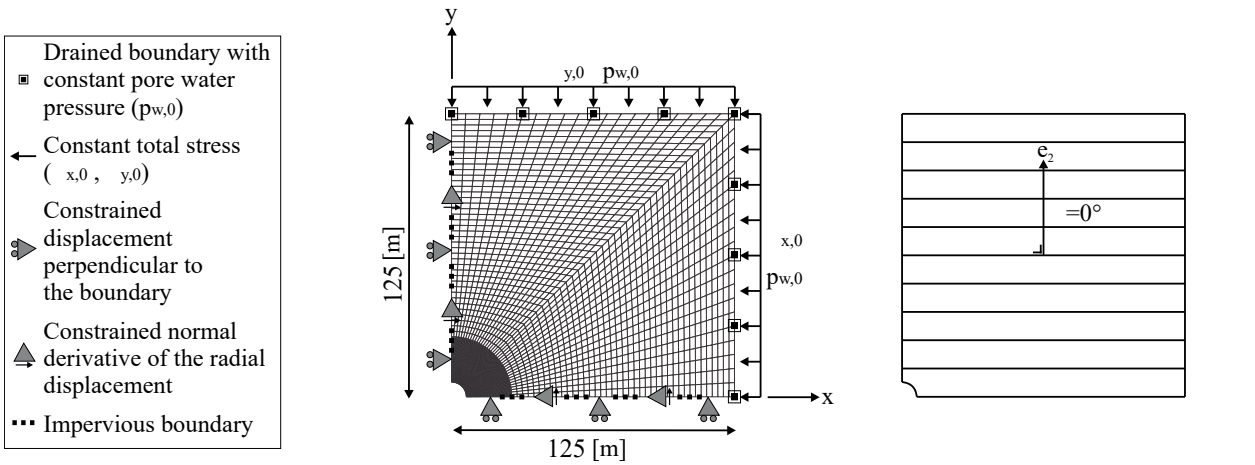

Fig. 7: Geometry and boundary conditions for the modelling of a gallery excavation in cross-anisotropic rock with horizontal bedding planes.

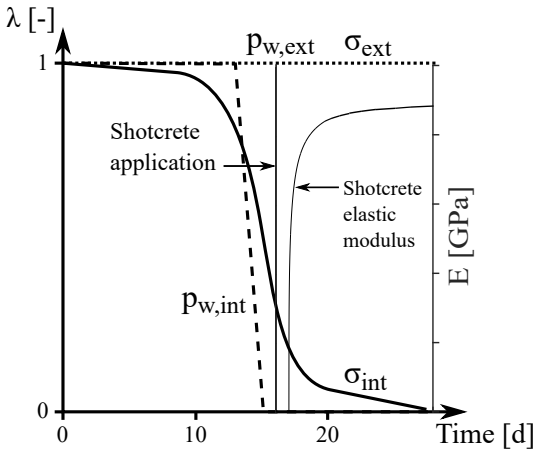

Fig. 8: Boundary conditions evolution. σ_{int} is the stress multiplier in the inside of the excavation, σ_{ext} in the outer boundary and P_w the pore pressure in the gallery wall. The elastic modulus of the shotcrete is added for comparison with the deconfining curve.

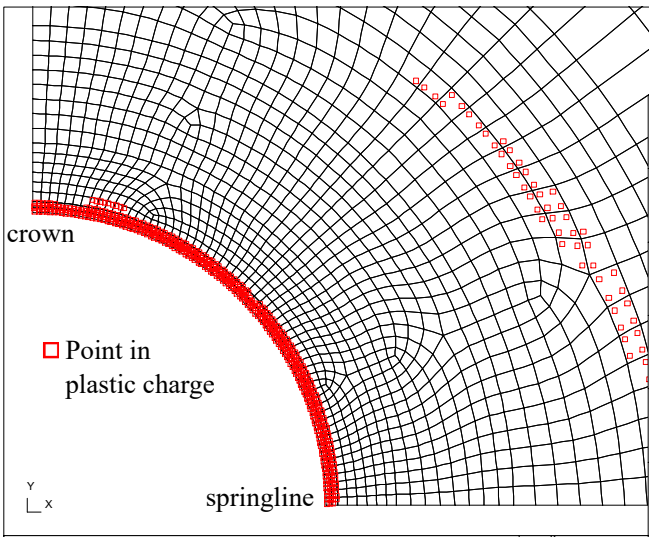

Fig. 9: Points in plastic charge at the end of the reference simulation.

The second invariant of strain (Figure 10) shows the strain localization in shear bands around the excavation with values up to 2.0%. The localization is not very concentrated presenting small shear bands in a wide area around the excavation. The effect of the shotcrete placed one day after the interception of the excavation front is likely to prevent the development of higher localization states.

The convergence plot (Figure 11) shows a fast convergence both in the springline and the crown of the excavation during the first 3 days due to the deconfinement rate and the hydration kinetics of the shotcrete which is placed one day after. After the day 4 the slope of the convergence rapidly decreases due to the increase of elastic modulus of the shotcrete and the excavation front moving away from the section. Finally around the day 13 the slope of the convergence evolution decreases again due to the end of deconfinement. After, the convergence continues slowly increasing due to the dissipation of pore pressure (primary consolidation) and progressively the long term more dominant viscous effects. The horizontal and vertical responses present an almost isotropic deformation, this is put down to the localization mode (Figure 10), which is strongly affected by the presence of shotcrete.

The stress path in the principal stresses $I_{\sigma'}$-$II_{\hat{\sigma}}$ plane (Figure 12) show the moment of application of the shotcrete

	Symbol	Name	Value	Unit
Hydraulic parameter	$k_{w\parallel 0}$	Initial parallel intrinsic water permeability	4×10^{-20}	m^2
	$k_{w\perp 0}$	Initial perpendicular intrinsic water permeability	1.33×10^{-20}	m^2
	Φ	Porosity	0.173	-
	$\mathcal{P}_r$	Van Genuchten air entry pressure	15	MPa
	$\mathcal{M}$	Van Genuchten material parameter	0.33	-
	S_{max}	Maximum degree of water saturation	1	-
	S_{res}	Residual degree of water saturation	0.01	-
	μ_w	Water dynamic viscosity	0.001	Pa s
	χ_w^{-1}	Water compressibility	5×10^{-10}	Pa^{-1}
Elastic parameters	$E_\parallel$	Parallel Young modulus	5	GPa
	$E_\perp$	Perpendicular Young modulus	4	GPa
	$G_{\parallel\perp}$	Shear modulus	1.63	GPa
	$\nu_\parallel$	Poisson's ratio	0.24	-
	$\nu_{\parallel\perp}$	Poisson's ratio	0.33	-
	$b_\parallel$	Parallel Biot's coefficient	0.60	-
	$b_\perp$	Perpendicular Biot's coefficient	0.64	-
	ρ_s	Solid grain density	2750	kg/m^3
	D	Second gradient elastic parameter	10.512	kN
Plastic parameters	η	Van Eekelen yield surface convexity parameter	-0.229	-
	$\psi_c = \psi_e$	Dilatancy angle in compression and extension	0.5	°
	ϕ_{c0}	Initial compression friction angle	10	°
	ϕ_{cf}	Final compression friction angle	23	°
	ϕ_{e0}	Initial extension friction angle	7	°
	ϕ_{ef}	Final extension friction angle	23	°
	B_ϕ	Friction angle hardening coefficient	0.001	-
	dec_ϕ	Friction angle hardening shifting	0	-
	$\bar{c}$	Cohesion for isotropic loading	4.1	MPa
	$A_\parallel$	Anisotropic cohesion parameter	0.117	-
	b_1	Anisotropic cohesion parameter	14.24	-
	ξ_c	Ratio of final to initial cohesion	5	-
	B_c	Cohesion softening coefficient	0.003	-
	dec_c	Cohesion softening shifting	0	-
Viscoplastic parameter	R_c	Uniaxial compressive strength	21	MPa
	A^{vp}	Internal friction coefficient	2.62	-
	C^{vp}	Cohesion coefficient	0.03	-
	β^{vp}	Viscoplastic potential parameter	1.1	-
	$g(\beta)$	Influence of the Lode angle	1	-
	α_0^{vp}	Initial threshold for viscoplastic flow	0.142	-
	γ_0	Reference fluidity	700	s^{-1}
	γ_1	Temperature parameter	57×10^3	J/mol
	$\mathcal{N}$	Creep curve shape parameter	5.0	-
	B^{vp}	Viscoplastic hardening parameter	0.03	-
Permeability Evolution	β_{per}	Permeability evolution parameter	10^{10}	-
	YI^{th}	Yield index threshold	0.95	-

Table 7: Physical parameters related to the mechanical constitutive laws, flow and hydro-mechanical couplings

and the start of ventilation for the crown and the springline.

4.3 Parametric study

In this subsection a parametric study is presented, the variables involved are accelerator agents in the concrete, time of the shotcrete spray and deformable wedges within the shotcrete liner. Gallery convergence plots are shown for the 44 days after the shotcrete spraying and the 3 parametric study cases are compared to the reference results.

4.3.1 Hydration accelerator

Accelerator additives are commonly used in sprayed shotcrete to accelerate the hardening [50]. The plots (Figure 13 and 14) show a very limited effect of the accelerator on the convergence.

The shotcrete with accelerator presents similar values of stiffness to its regular version roughly 4 hours before. This anticipation causes the host rock to release more stress into the shotcrete slightly decreasing the convergence with respect the regular case after the day 4. The convergence reduction is only 0.5mm after 44 days. The shotcrete orthoradial stress is $43.0MPa$

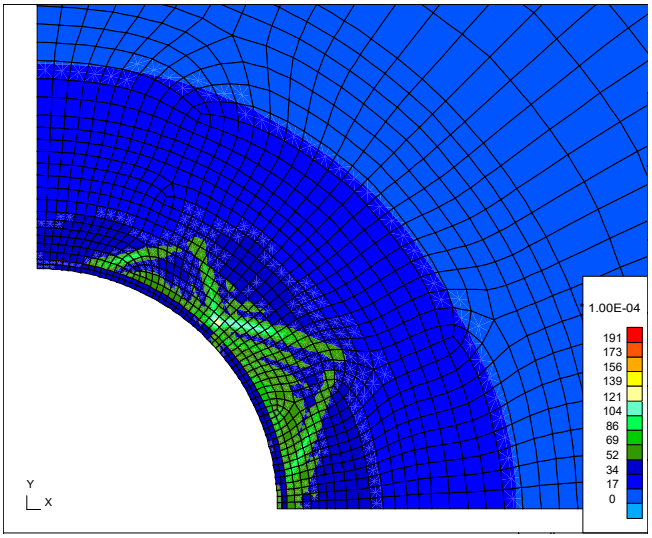

Fig. 10: Total second invariant of strain at the end of the reference simulation.

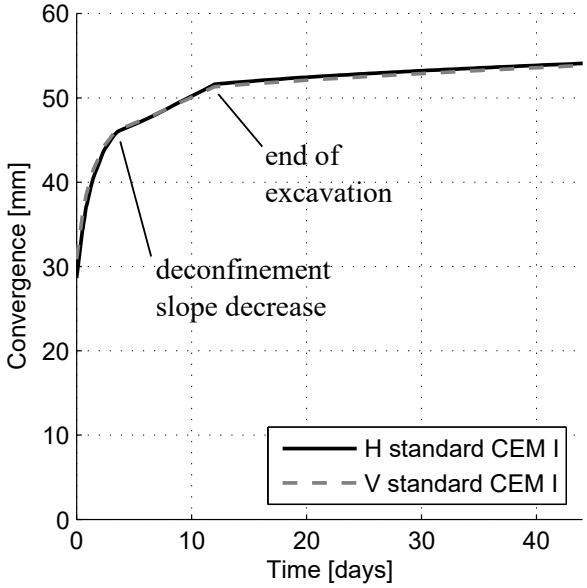

Fig. 11: Horizontal and vertical convergence of the gallery 44 days after the shotcrete. Reference simulation.

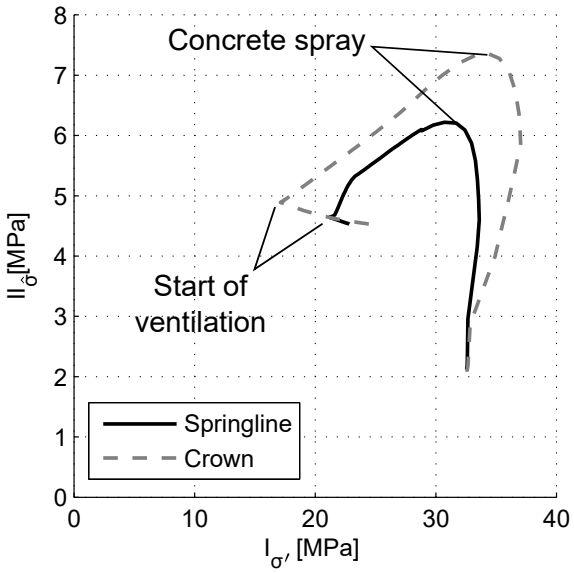

Fig. 12: Springline and crown COX effective stress evolution in the I_σ-II_σ plane.

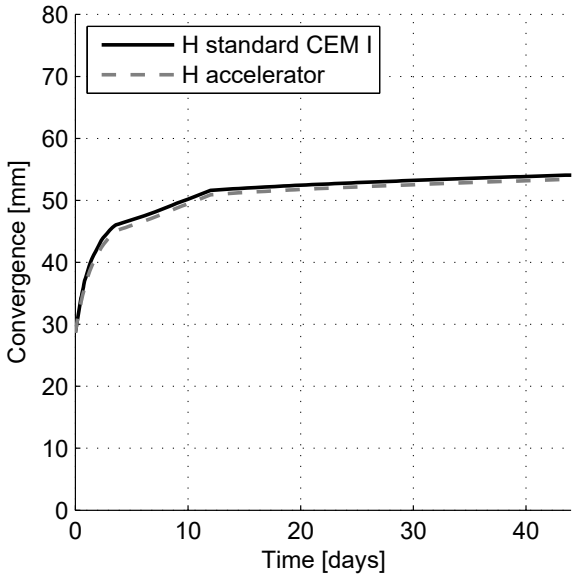

Fig. 13: Horizontal convergence in the springline of the excavation for 2 different hydratation velocities.

in the springline and 46.1MPa in the crown, slightly higher than the ones of the reference case.
The points in plastic charge in Figure 15 show that the rock is mostly not in plastic charge while the shotcrete is in plastic charge due to the high stress of this. The deformation isotropy can be put down to the localization mode (Figure 16) which is sensibly similar to the one of the reference case (Figure 10).
The total deconfinement of the initial stresses requires almost 30 days, as reported in Figure 8. Therefore the gain of 4 hours to obtain a similar stiffness does not significantly impact the convergence.

4.3.2 Delayed application

A common technique to adjust the stress in concrete liners in tunnel excavations is to delay the application of

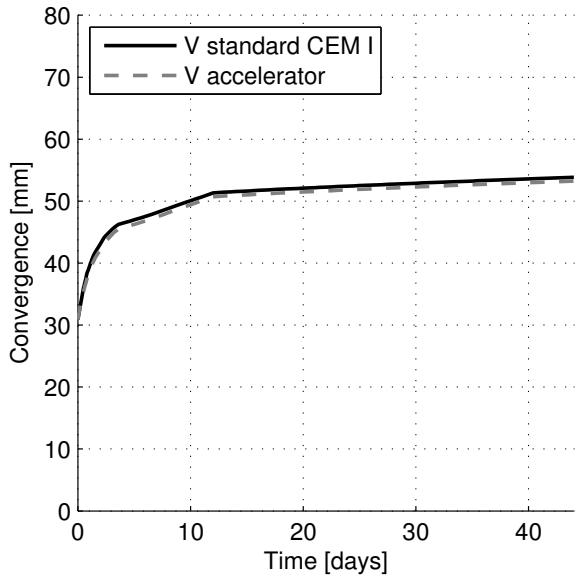

Fig. 14: Vertical convergence in the crown of the excavation for 2 different hydratation velocities.

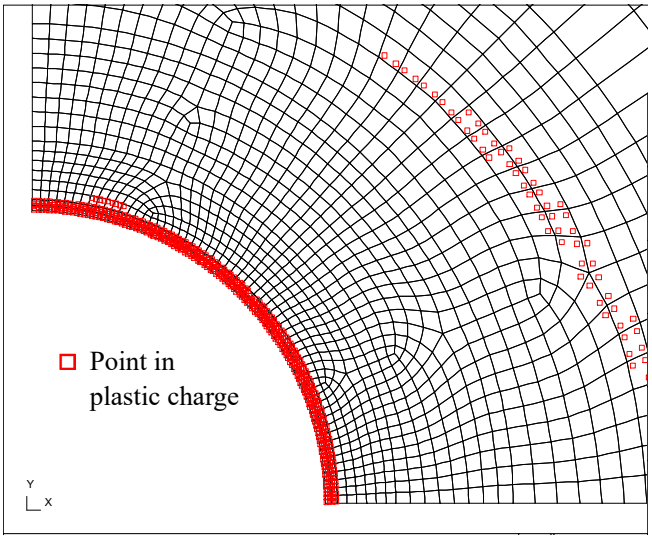

Fig. 15: Hydration accelerator: points in plastic charge at 44 days.

the concrete to allow some deformation of the rock [38]. Subsequently deformation of the gallery section generates an orthoradial stress distribution acting as a vault arch. Once the concrete is placed, it is less loaded due to the contribution of the rock. This allows economies in the supporting structure by reducing its dimensions or using a lower specification concrete.

The plots in Figure 17 correspond to simulations where shotcrete is applied one day (reference) or six days (delayed) after excavation. The delayed application of shotcrete has a much bigger impact on the gallery

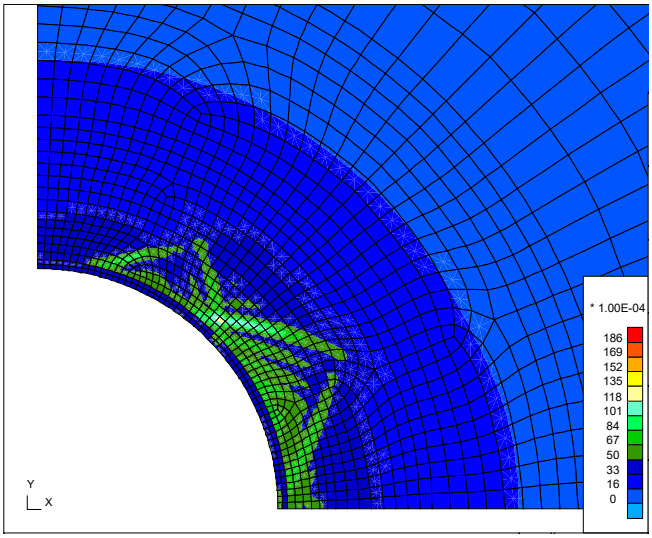

Fig. 16: Hydration accelerator: total second invariant of strain at 44 days.

convergence than in the previous case. It increases by 16mm in the horizontal direction and 10mm in the vertical. The shotcrete orthoradial stress is $18.2MPa$ in the springline and $20.8MPa$ in the crown, which is sensibly lower than the reference case.

The points in plastic charge in Figure 18 show different results compared to the reference simulation and the case with accelerator; the rock presents shear banding 19 with some plastification in the bands while the shotcrete layer remains in the elastic region.

Contrary to the reference simulation, the delayed application of shotcrete leads to an anisotropic deformation of the gallery where horizontal deformation becomes larger than the vertical one, as reported in Figure 17. This can be explained because of the development of a different localization mode (Figure 19) with much higher value of the second invariant of strain: maximum of 5% compared to the 2% of the reference or the accelerator case.

4.3.3 Deformable wedges

The reference simulation exhibits that applying shotcrete after one day gives birth to very high stress within concrete and limits convergence. On the other hand delaying the application of the shotcrete is an effective way to reduce the solicitation, but it leaves the excavation unprotected against the fall of rock blocks during the delay period. A second option to reduce the solicitation without delaying the application of the shotcrete is to include deformable wedges within the shotcrete layer. These parts have the mission of absorbing big deformations while not surpassing a threshold of stress.

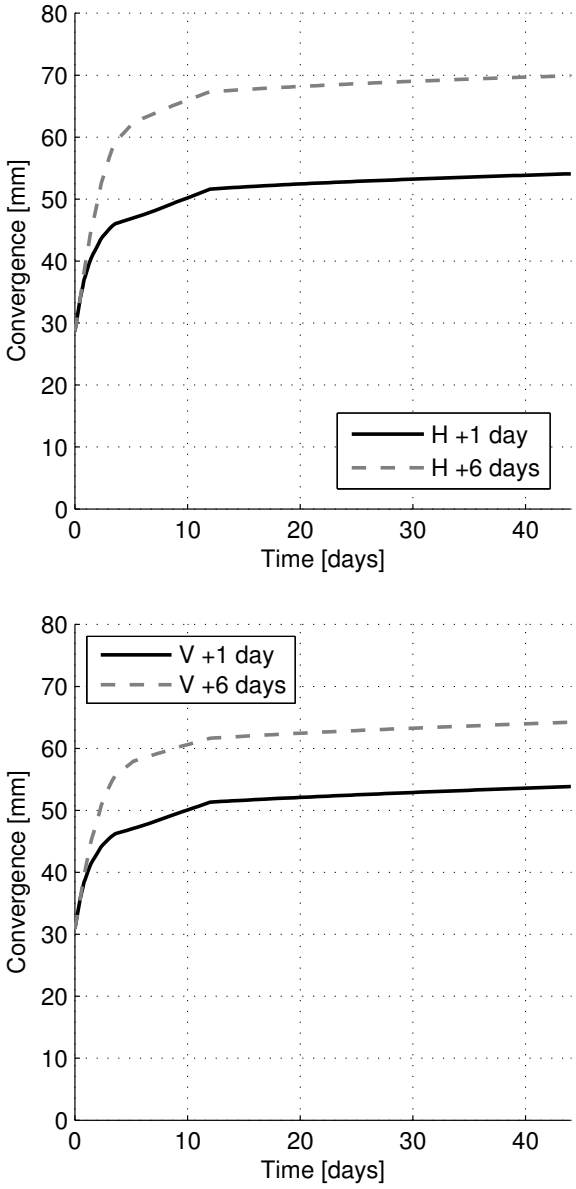

Fig. 17: a) Horizontal convergence in the springline of the excavation for 2 different shotcrete application times.

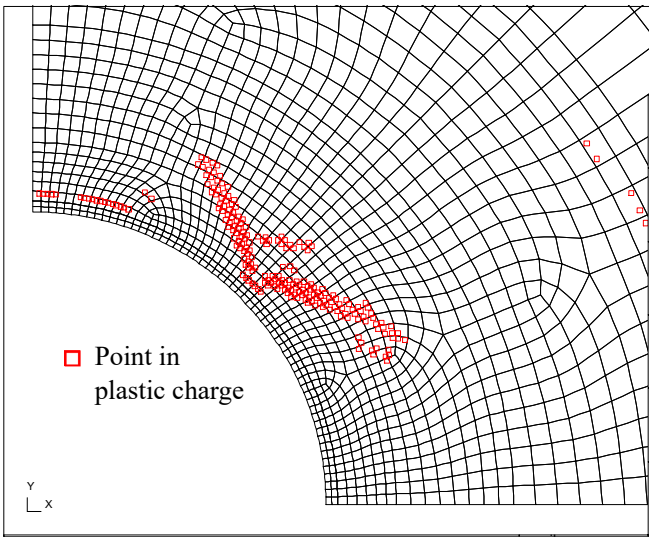

Fig. 18: Delayed application: points in plastic charge at 44 days.

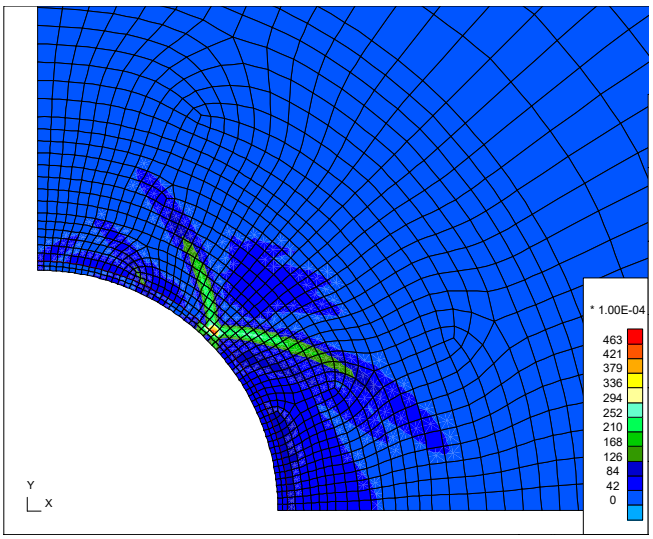

Fig. 19: Delayed application: total second invariant of strain at 44 days.

They consist in a perfectly plastic mechanism modelled as a purely cohesional Tresca material: elastic modulus $E = 1GPa$ and cohesion $c = 2.5MPa$. From a practical point of view, these elements are already present in the concrete support FEM mesh when the shotcrete starts the hydration.

Figure 20 corresponds to the reference simulation, with a continuous shotcrete vault, and a simulation with two deformable wedges in the quarter of the circumference. The deformation allowed by the wedges greatly increases the excavation convergence and reduces the shotcrete stress. The convergence increases by 38mm in the horizontal direction and 20mm in the vertical. The shotcrete orthoradial stress is $17.8MPa$ in the springline and $18.0MPa$ in the crown, values sensibly lower compared to the ones of the reference case.

In this case, similarly to the case with a delayed application of shotcrete, the plastic charge occurs in the rock rather than the shotcrete (Figure 21) due to the low stress taken by this last. The points in plastic charge follow the localization network predefined by the position of the compressible wedges. The deformable wedges are also in plastic charge since they are constituted by a

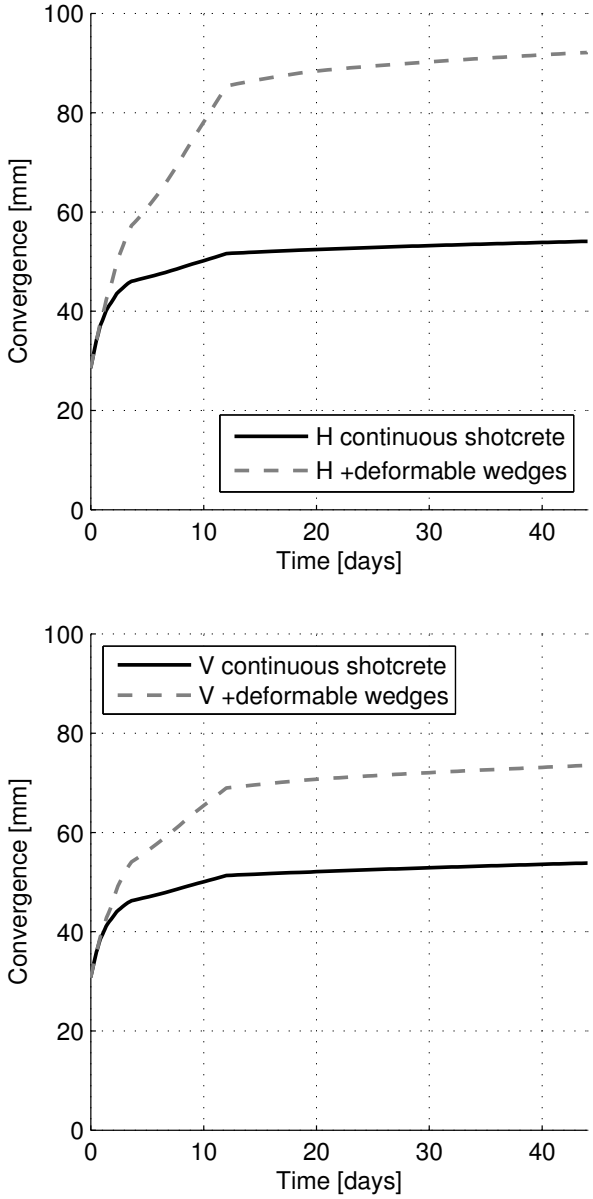

Fig. 20: Horizontal and vertical convergence in the springline of the excavation using continuous shotcrete vs. compressible wedges to release stress in the shotcrete.

low elastic modulus perfectly plastic material that takes most of the deformation of the shotcrete layer.

With the use of deformable wedges the deformation anisotropy is even more accentuated than in the previous case with a higher horizontal deformation (Figure 22). Once more this is put down to the localization mode, which is different to all the previous. The deformable wedges create a concentration of deformation in the inner part of the excavation that triggers the localization of deformation.

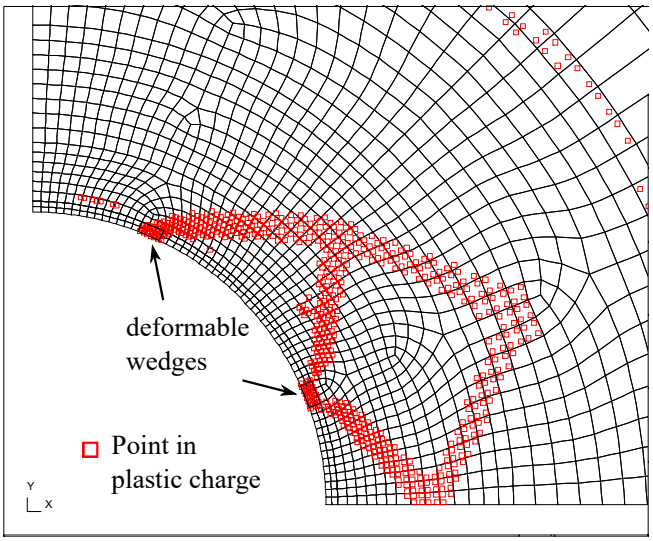

Fig. 21: Deformable wedges: points in plastic charge at 44 days.

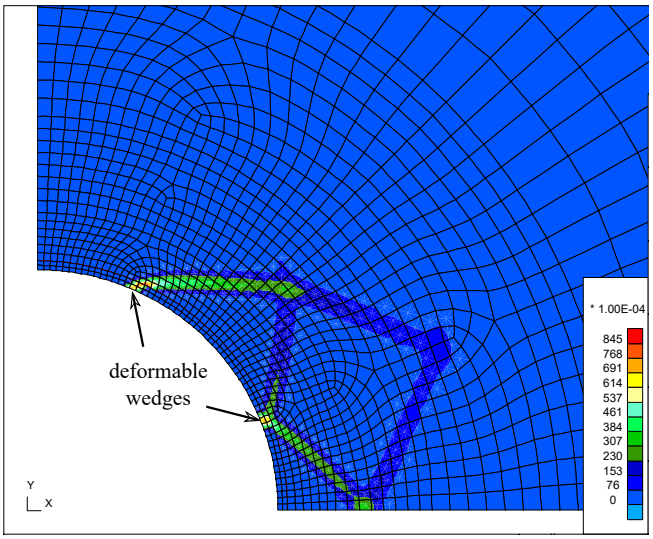

Fig. 22: Deformable wedges: total second invariant of strain at 44 days.

4.3.4 Stress evolution

The orthoradial stress evolution in the crown of the shotcrete layer is presented in Figure 23. The stress boundary condition is zero in the radial direction, this means that the orthoradial can be directly compared

to the simple compression strength of the shotcrete to evaluate its limit status.

Two groups of behaviours can be observed: one in which the concrete reaches high stress levels (reference simulation and accelerator case) and another one in which the concrete stress is lower and more deformation and plasticity happen within the rock (delayed application and deformable wedge cases). In the second group a distinction can be made. For the delayed application, the shotcrete takes less stress due to the time shift that lets the rock deform without any restriction. While for the deformable wedges, there is no time shift but a decrease of the overall supporting structure stiffness.

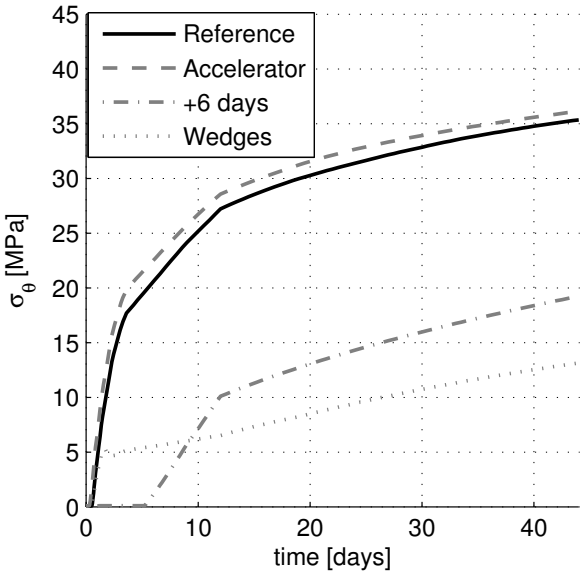

Fig. 23: Crown orthoradial stress evolution, reference simulation and all the parametric cases.

Similarly, the horizontal convergence is close for the reference case and the accelerator and higher for the other two cases; the delayed application reaches higher levels at early time, but after 6 days it is the case with deformable wedges that presents the larger convergence values (figure 24).

A combination of those techniques can be used to obtain the desired convergence and stress levels according to the rock and excavation characteristics. It allows to optimise the proposed solution with respect to the cost and structure safety.

The following tables (Table 8 and 9) summarize the convergences and orthoradial stresses after 44 days. The convergence values (Table 8) show an important increase of convergence for the delayed application and this has a higher anisotropic component due to the

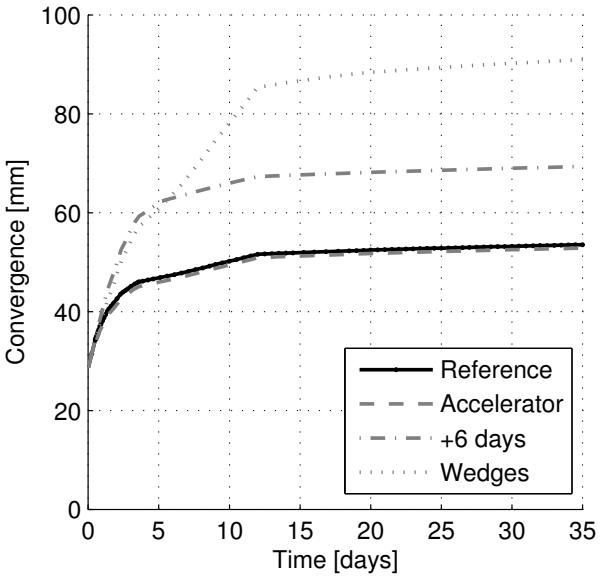

Fig. 24: Springline horizontal convergence evolution, reference simulation and all the parametric cases.

higher development of localization. Similarly, the case with deformable wedges presents yet larger convergence and anisotropy due to localization in shear bands. In this later case the shear bands are triggered by the wedge position.

Convergence [mm]	springline	crown
Reference	54.1	53.8
Accelerator	53.5	53.5
Spraying at +6 days	69.9	64.2
Deformable wedges	92.1	73.5

Table 8: Summary of the rock wall convergences in the springline and crown at 44 days for the different parametric cases

The orthoradial stresses (Table 9) present similar values for the reference and accelerator cases while for the delayed case and with wedges the stress is less than half. Note that the orthoradial stress distribution along the shotcrete circumference is strongly variable due to the presence of the wedges. The crown and springline are exactly in the middle between two wedges so the stress value is the maximum found along the shotcrete. The other cases present much more homogeneous stress along the shotcrete circumference so the values in the crown and springline can be used as averaging values.

Orthoradial stress [MPa]	springline	crown
Reference	45.1	42.5
Accelerator	43.0	46.1
Spraying at +6 days	18.2	20.8
Deformable wedges	17.8	18.0

Table 9: Summary of the shotcrete effective orthoradial in the springline and crown at 44 days for the different parametric cases

5 Conclusions

In this work we investigated the short-term interactions between the support structure and the host rock in the context of deep underground nuclear waste storage. Hydro-mechanically coupled finite element simulations of the excavation process are coupled with the modelling of early age concrete of the support structure. The selected case study is a 10.4m diameter gallery designed to storage long-lived intermediate-level waste (MAVL). The behaviour of the rock is captured by the combination of a complex constitutive mechanical model including stiffness and strength orthotropic anisotropy, hardening of the friction angle, softening of the cohesion, Lode angle dependency and viscoplastic effects. It is coupled with an anisotropic deformation dependant flow model, encompassing partial saturation effects.
Early age concrete behaviour is decoupled from the excavation phase by solving the adiabatic hydration equations from initial conditions representative of the tunnel. The resulting time evolution of the hydration degree is used as an input for the finite element simulation of the boundary value problem. Assuming a constant friction angle, the cohesion of the concrete material is linked to its hydration degree.
Four different configurations are compared with respect to the development of orthoradial stress in the support structure and convergence of the gallery. The reference simulation assumes shotcrete is applied one day after excavation is complete. The first variant assumes additive accelerate the shotcrete hydration. Another simulation assesses the effect of a delayed projection (6 days after excavation) of the shotcrete. Finally deformable wedges are inserted into the support.
Results indicate that two basic variables must be taken into account for the gallery design. The reference and accelerated simulations both exhibit the lowest convergence of the host rock but high orthoradial stresses develop in the concrete. On the contrary delayed shotcrete projection and deformable wedge lead to lower stress at the cost of a larger deformation.
The support solution strongly influences the localisation pattern and extent within the surrounding rock. The reference and accelerated solutions exhibit a more diffuse damaging of the rock while the last two solutions lead to very distinct localisation shear bands. In addition plastic wedges trigger localisation bands at their respective positions.
This work opens new perspectives on the topic since the model can still be improved. Taking into account early age creep is one of the hypotheses that could affect results. This should be taken into account through an appropriate model but requires more experimental results to be validated. In addition the full coupling of hydration phenomena and environment, might influence the interactions between concrete and host rock. Especially temperature and water exchange might be considered.

References

1. Agency, I. A. E. From Obninsk Beyond: Nuclear Power Conference Looks to Future. `https://www.iaea.org/newscenter/news/obninsk-beyond-nuclear-power-conference-looks-future`, 2004. Accessed: 2010-11-21.
2. Agency, O. N. E. The environmental and ethical basis of geological disposal of longlived radioactive wastes. A collective opinion of the Radioactive Waste Management Committee of the OECD Nuclear Energy Agency. *Technical report* (1995).
3. Andra, D. Evaluation of the feasibility of a geological repository in an argillaceous formation. *Andra, Chatenay-Malabry, France* (2005).
4. Armand, G., Leveau, F., Nussbaum, C., de La Vaissiere, R., Noiret, A., Jaeggi, D., Landrein, P., and Righini, C. Geometry and properties of the excavation-induced fractures at the meuse/haute-marne url drifts. *Rock Mechanics and Rock Engineering 47*, 1 (2014), 21–41.
5. Benboudjema, F., and Torrenti, J. M. Early-age behaviour of concrete nuclear containments. *Nuclear Engineering and Design 238*, 10 (2008), 2495–2506.
6. Blümling, P., Bernier, F., Lebon, P., and Martin, C. D. The excavation damaged zone in clay formations time-dependent behaviour and influence on performance assessment. *Physics and Chemistry of the Earth, Parts A/B/C 32*, 8 (2007), 588–599.
7. Briffaut, M., Benboudjema, F., Torrenti, J.-M., and Nahas, G. Concrete early age basic creep: Experiments and test of rheological modelling approaches. *Construction and Building Materials 36* (2012), 373–380.
8. Bryne, L. *Time Dependent Material Properties of Shotcrete for Hard Rock Tunneling.* PhD thesis, KTH Stockholm, 2014.
9. Bryne, L., Ansell, A., and Holmgren, J. Laboratory testing of early age bond strength of shotcrete on hard rock. *Tunnelling and Underground Space Technology 41*, 1 (2014), 113–119.
10. Buffo-Lacarrière, L., and Sellier, A. Chemo-mechanical modeling requirements for the assessment of concrete structure service life. *Journal of Engineering Mechanics 137*, 9 (2011), 625–633.
11. Buffo-Lacarrière, L., Sellier, A., Escadeillas, G., and Turatsinze, A. Multiphasic finite element modeling

of concrete hydration. *Cement and Concrete Research 37*, 2 (2007), 131–138.

12. Buffo-Lacarrière, L., Sellier, A., Turatsinze, A., and Escadeillas, G. Finite element modelling of hardening concrete: application to the prediction of early age cracking for massive reinforced structures. *Materials and Structures 44*, 10 (2011), 1821–1835.
13. Chambon, R., Caillerie, D., and El Hassan, N. One-dimensional localisation studied with a second grade model. *European Journal of Mechanics-A/Solids 17*, 4 (1998), 637–656.
14. Charlier, R. *Approche unifié de quelques problèmes non linéaires de mécanique des milieux continus par la méthode des éléments finis (grandes déformations des métaux et des sols, contact unilatéral de solides, conduction thermique et écoulements en milieu poreux)*. PhD thesis, University of Liege, 1987.
15. Charron, J.-P., Marchand, J., Bissonnette, B., and Gérard, B. Étude comparative de modèles phénoménologiques décrivant le comportement au jeune âge du béton. Partie 1 . *Canadian Journal of Civil Engineering 28*, 2 (2001), 323–331.
16. Charron, J.-P., Marchand, J., Bissonnette, B., and Gérard, B. Étude comparative de modèles phénoménologiques décrivant le comportement au jeune âge du béton. Partie 2. *Canadian Journal of Civil Engineering 28*, 2 (2001), 323–331.
17. Chen, L., Shao, J.-F., and Huang, H. Coupled elastoplastic damage modeling of anisotropic rocks. *Computers and Geotechnics 37*, 1 (2010), 187–194.
18. Cheng, A.-D. Material coefficients of anisotropic poroelasticity. *International Journal of Rock Mechanics and Mining Sciences 34*, 2 (1997), 199–205.
19. Collin, F. *Couplages thermo-hydro-mécaniques dans les sols et les roches tendres partiellement saturés*. PhD thesis, Université de Liège, Liège, Belgique, 2003.
20. Collin, F., Caillerie, D., and Chambon, R. Analytical solutions for the thick-walled cylinder problem modeled with an isotropic elastic second gradient constitutive equation. *International Journal of Solids and Structures 46*, 22 (2009), 3927–3937.
21. Collin, F., Chambon, R., and Charlier, R. A finite element method for poro mechanical modelling of geotechnical problems using local second gradient models. *International journal for numerical methods in engineering 65*, 11 (2006), 1749–1772.
22. De Schutter, G. Degree of hydration based Kelvin model for the basic creep of early age concrete. *Materials and Structures 32*, May (1999), 260–265.
23. De Schutter, G., and Taerwe, L. Degree of hydration-based description of mechanical properties of early age concrete. *Materials and Structures 29*, 6 (1996), 335–344.
24. Feiveson, H., Mian, Z., Ramana, M., and von Hippel, F. Managing nuclear spent fuel: Policy lessons from a 10-country study. *Bulletin of the Atomic Scientists 27* (2011).
25. Félix, B., Lebon, P., Miguez, R., and Plas, F. A review of the andra's research programmes on the thermo-hydromechanical behavior of clay in connection with the radioactive waste disposal project in deep geological formations. *Engineering geology 41*, 1-4 (1996), 35–50.
26. Galli, G., Grimaldi, A., and Leonardi, A. Three-dimensional modelling of tunnel excavation and lining. *Computers and Geotechnics 31*, 3 (2004), 171–183.
27. Gawin, D., Pesavento, F., and Schrefler, B. A. Modelling creep and shrinkage of concrete by means of effective stresses. *Materials and Structures 40*, 6 (2007), 579–591.
28. Germain, P. La méthode des puissances virtuelles en mécanique des milieux continus. *J. Mécanique 12* (1973), 236–274.
29. Gutsch, a. Properties of early age concrete - Experiments and modelling. *Materials and Structures 35*, 246 (2002), 76–79.
30. Hajiabdolmajid, V., and Kaiser, P. Brittleness of rock and stability assessment in hard rock tunneling. *Tunnelling and Underground Space Technology 18*, 1 (2002), 35–48.
31. Hellmich, C., Sercombe, J., Ulm, F.-J., and Mang, H. Modeling of early-age creep of shotcrete. II: application to tunneling. *Journal of Engineering Mechanics 126*, MARCH (2000), 292–299.
32. Hilaire, A., Benboudjema, F., Darquennes, A., Berthaud, Y., and Nahas, G. Modeling basic creep in concrete at early-age under compressive and tensile loading. *Nuclear Engineering and Design 269* (2014), 222–230.
33. Jia, Y., Bian, H., Duveau, G., Su, K., and Shao, J.-F. Hydromechanical modelling of shaft excavation in meuse/haute-marne laboratory. *Physics and Chemistry of the Earth, Parts A/B/C 33* (2008), S422–S435.
34. Khalili, N., Habte, M., and Zargarbashi, S. A fully coupled flow deformation model for cyclic analysis of unsaturated soils including hydraulic and mechanical hystereses. *Computers and Geotechnics 35*, 6 (2008), 872–889.
35. Khoshghalb, A., and Khalili, N. A meshfree method for fully coupled analysis of flow and deformation in unsaturated porous media. *International Journal for Numerical and Analytical Methods in Geomechanics 37*, 7 (2013), 716–743.
36. Kim, J., Ryu, J., and Hooton, R. Evaluation of strength and set behavior of mortar containing shotcrete set accelerators. *Canadian Journal of Civil Engineering 35*, 4 (2008), 400–407.
37. Kolani, B., Buffo-Lacarrière, L., Sellier, A., Escadeillas, G., Boutillon, L., and Linger, L. Hydration of slag-blended cements. *Cement and Concrete Composites 34*, 9 (2012), 1009–1018.
38. Leca, E. *Analysis of NATM and shield tunneling in soft ground*. PhD thesis, Virginia Polytechnic Institute and State University, 1989.
39. Martin, C., and Chandler, N. The progressive fracture of lac du bonnet granite. *International Journal of Rock Mechanics and Mining Sciences & Geomechanics Abstracts 31*, 6 (1994), 643–659.
40. Meschke, G. Consideration of aging of shotcrete in the context of a 3D viscoplastic material model. *International Journal for Numerical in Engineering 39*, 3 (1996), 3123–3143.
41. Olivella, S., Gens, A., Carrera, J., and Alonso, E. Numerical formulation for a simulator (code_bright) for the coupled analysis of saline media. *Engineering computations 13*, 7 (1996), 87–112.
42. Oreste, P., and Pella, D. Modelling progressive hardening of shotcrete in convergence-confinement approach to tunnel design. *Tunnelling and Underground Space Technology 12*, 3 (1997), 425–431.
43. Panet, M., and Guenot, A. Analysis of convergence behind the face of a tunnel: Tunnelling 82, proceedings of the 3rd international symposium, brighton, 7–11 june

1982, p197–204. publ london: Imm, 1982. In *International Journal of Rock Mechanics and Mining Sciences & Geomechanics Abstracts* (1983), vol. 20, Pergamon, p. A16.
44. Pardoen, B. *Hydro-mechanical analysis of the fracturing induced by the excavation of nuclear waste repository galleries using shear banding.* PhD thesis, University of Liege, 2015.
45. Pardoen, B., and Collin, F. Modelling the influence of strain localisation and viscosity on the behaviour of underground drifts drilled in claystone. *Computers and Geotechnics 85* (2017), 351–367.
46. Pardoen, B., Talandier, J., and Collin, F. Permeability evolution and water transfer in the excavation damaged zone of a ventilated gallery. *International Journal of Rock Mechanics and Mining Sciences 85* (2016), 192–208.
47. Perzyna, P. Fundamental problems in viscoplasticity. *Advances in applied mechanics 9* (1966), 243–377.
48. Pietruszczak, S., Lydzba, D., and Shao, J.-F. Modelling of inherent anisotropy in sedimentary rocks. *International Journal of Solids and Structures 39*, 3 (2002), 637–648.
49. Pietruszczak, S., and Pande, G. Description of soil anisotropy based on multi-laminate framework. *International journal for numerical and analytical methods in geomechanics 25*, 2 (2001), 197–206.
50. Prudêncio, L. R. Accelerating admixtures for shotcrete. *Cement and Concrete Composites 20*, 2-3 (1998), 213–219.
51. Sellier, A., Multon, S., Buffo-Lacarrière, L., Vidal, T., Bourbon, X., and Camps, G. Concrete creep modelling for structural applications: Non-linearity, multi-axiality, hydration, temperature and drying effects. *Cement and Concrete Research 79* (2016), 301–315.
52. Sercombe, J., Hellmich, C., Ulm, F.-J., and Mang, H. Modeling of early-age creep of shotcrete. I: model and model parameters. *Journal of Engineering Mechanics 126*, March (2000), 284–291.
53. Tazawa, E.-I., and Miyazawa, S. Influence of cement and admixture on autogenous shrinkage of cement paste. *Cement and Concrete Research 25*, 2 (1995), 281–287.
54. van Breugel, K. Numerical simulation of hydration and microstructural development in hardening cement-based materials. (I) theory. *Cement and Concrete Research 25*, 2 (1995), 319–331.
55. Van Eekelen, H. Isotropic yield surfaces in three dimensions for use in soil mechanics. *International Journal for Numerical and Analytical Methods in Geomechanics 4*, 1 (1980), 89–101.
56. Van Genuchten, M. T. A closed-form equation for predicting the hydraulic conductivity of unsaturated soils. *Soil science society of America journal 44*, 5 (1980), 892–898.
57. Won, J., Hwang, U.-J., Kim, C., and Lee, S. Mechanical performance of shotcrete made with a high-strength cement-based mineral accelerator. *Construction and Building Materials 49* (2013), 175–183.
58. Zhou, H., Jia, Y., and Shao, J.-F. A unified elastic–plastic and viscoplastic damage model for quasi-brittle rocks. *International Journal of Rock Mechanics and Mining Sciences 45*, 8 (2008), 1237–1251.